Research Square

Preprints are preliminary reports that have not undergone peer review.
They should not be considered conclusive, used to inform clinical practice,
or referenced by the media as validated information.

An insect-scale quadruped robot with a mechanically coupled transmission for confined environments

Yide Liu

yide_liu@zju.edu.cn

Tsinghua University https://orcid.org/0000-0002-2447-3107

Rui Chen

Bian Gan

Zhejiang University

Bo Feng

Zhejiang University https://orcid.org/0000-0003-1780-7559

Shaoxing Qu

Zhejiang University https://orcid.org/0000-0002-1217-4644

Article

Keywords:

Posted Date: November 9th, 2026

DOI: https://doi.org/10.21203/rs.3.rs-11571811/v1

License: This work is licensed under a Creative Commons Attribution 4.0 International License.
Read Full License

Additional Declarations: There is **NO** Competing Interest.

Abstract

Insect-scale robots hold promise for exploration and rescue in confined environments, yet achieving simultaneous fast locomotion, high payload capacity, and long endurance under severe mass and volume constraints remains a fundamental challenge. Here, we present a 20.9 g, 6 cm insect-scale quadruped robot enabled by a mechanically coupled single-degree-of-freedom transmission. By tuning the transmission ratio, we engineered two distinct configurations. The high-torque variant utilizes a three-stage gearbox to transport up to 250 g—12 times its own weight—and sustains a 12 N quasi-static load, while the standard configuration achieves a forward speed of 36.9 cm/s. Operating untethered with wireless control, the robot completes more than 400 m of continuous locomotion. Furthermore, it successfully executes teleoperated pickup-and-return tasks within physically confined spaces. These results establish a mechanically coordinated design strategy that links high agility, load-bearing capacity and task-level integration at insect scale.

Introduction

Confined, unstructured environments are a compelling application domain for insect-scale mobile robots because small bodies can access low-clearance openings, narrow passages, and locally obstructed spaces that are inaccessible to larger platforms. Miniaturization, however, makes system integration increasingly restrictive. Motors, transmissions, batteries, electronics, sensing, communication, and task hardware must share a limited mass and volume budget, while the supporting structure must withstand locomotion-induced impacts and externally carried loads. A useful field-oriented platform therefore must do more than achieve high locomotion speed: it must provide sufficient structural capacity and integration space for perception, control, power, communication, and task interaction without making the locomotion system prohibitively complex.

Insect-scale terrestrial robots have demonstrated high normalized speeds, untethered or autonomous operation, shape adaptation, multimodal locomotion, and substantial robustness[1–18]. HAMR, DASH, RoACH, S²worm, S²worm-G, and BHMbot illustrate different approaches to compact and rapid legged locomotion[1–7], whereas CLARI and mCLARI emphasize passive or actively exploited body-shape adaptation for laterally confined spaces[9,10]. Soft, piezoelectric, and multimodal microrobots further extend the achievable design space in payload transport, environmental adaptability, and mechanical robustness[11–18]. These systems demonstrate strong individual capabilities, but simultaneously integrating load-bearing structures, onboard visual and inertial feedback, wireless control, power, and task hardware remains difficult at insect scale. This integration challenge motivates locomotion architectures that reduce the number of actively coordinated variables while preserving useful three-dimensional foot motion and structural load paths.

Transmission architecture is central to this tradeoff. Existing small-scale legged robots span a spectrum from mechanisms with multiple compliant actuation inputs with substantial trajectory-control capability to lower-dimensional linkage-based transmissions with reduced actuation complexity. HAMR employs

flexure-based spherical five-bar (SFB) mechanisms that combine leg lifting and fore-aft swing to generate controlled foot trajectories at high operating frequencies[1,2]. This architecture provides substantial control over leg motion but retains multiple independently driven actuation inputs and associated phase-coordination requirements. RoACH follows a different approach, using smart composite microstructure (SCM) flexure hinges and composite links together with two shape-memory-alloy (SMA) inputs and a hip parallelogram/four-bar linkage to convert actuator motion into fore-aft swing and lifting[4]. The resulting architecture facilitates compact onboard integration and reduces mechanical complexity, although the foot trajectory is more strongly constrained by the linkage geometry and the attainable actuation bandwidth is limited by the thermal response of the SMA actuators.

S²worm and S²worm-G use three-chain, two-DOF parallel/origami transmissions to produce coupled lifting and torsional motion of a moving platform, demonstrating that parallel mechanisms can provide compact spatial foot motion at insect scale[5,6]. The present design builds on this type of parallel transmission but removes the need to command its two input branches independently. We introduce an upstream crank-rocker and impose a fixed mechanical relationship between the parallel-mechanism inputs, thereby reducing the actuation dimensionality of the transmission: one continuous rotary input maps directly to a periodic three-dimensional foot trajectory. This choice deliberately trades real-time trajectory adjustability for fewer independently driven inputs, less wiring, and reduced phase-coordination requirements. Smart composite microstructures (SCMs) then serve not only as a lightweight fabrication approach but also as the rigid-flex structural backbone that preserves transmission geometry, carries external and onboard loads, and provides mounting interfaces for sensing, power, communication, and task modules[19]. The resulting transmission is therefore intended not simply to reduce actuator count, but to provide a mechanically coordinated locomotion base compatible with system-level integration at insect scale.

Task-capable small robots impose additional integration requirements because sensing and interaction hardware directly consume the same payload and power budgets needed for locomotion. Previous miniature systems have incorporated grippers, magnetic actuation, or environmental sensors to extend locomotion platforms toward manipulation and field-oriented functions[20–23]. Here, rather than pursuing dexterous manipulation, we use a lightweight ventral magnetic module that reduces object interaction to an approach-attach-transport-return sequence. The module attaches magnetically to a ferromagnetic target, trading generality for minimal mass and control effort, and makes it possible to evaluate object interaction together with onboard visual feedback, attitude sensing, wireless communication, and locomotion within the same insect-scale system.

We present an insect-scale quadruped robot built around this single-degree-of-freedom (DOF) coupled transmission. The study contributes at three levels. First, we develop a 6-cm platform with a 9.90-g mechanical structure and a baseline task-integrated mass of approximately 20.9 g, combining locomotion actuation, onboard power, inertial sensing, visual feedback, wireless communication, and a

lightweight magnetic task module. Second, the crank-rocker/parallel-mechanism coupling allows one continuous rotary input to generate a closed three-dimensional foot trajectory while reducing the number of independently driven transmission inputs and associated phase-coordination variables. Third, we evaluate the platform from transmission-level kinematic output to integrated operation through geometric trajectory validation, baseline locomotion and turning, slope traversal, dynamic payload transport, multi-prototype quasi-static compression, multi-terrain traversal, teleoperated open-area mobility, repeated approximately 407-m runs, and a confined test-tube pickup-and-return task. Together, these experiments show that low-dimensional mechanical coordination can serve as a load-bearing, integrable locomotion base for a task-oriented insect-scale robot, and they define the conditions under which that strategy outperforms single-metric optimization.

Results

Platform architecture and operating configurations

The robot uses a symmetric quadruped layout constructed as an SCM rigid-flex frame (Fig. 1A, B, and Supplementary Fig. 1). The purely mechanical structure weighs 9.90 g. The baseline task-integrated prototype, including the controller, motor drivers, nine-axis inertial measurement unit (IMU), complementary metal-oxide-semiconductor (CMOS) camera, 60 mAh battery, and magnetic module, weighs approximately 20.9 g and has a characteristic body length of approximately 6 cm; the corresponding component mass breakdown is shown in Fig. 1C. The SCM body provides transmission alignment, load support, and mounting interfaces, while the camera and IMU provide visual and attitude information and the ESP32 handles motor control, sensing, and wireless communication. The prototype layout and onboard integration are shown in Fig. 1 and Supplementary Fig. 1.

Unless otherwise stated, experiments used 610 coreless motors, a single-stage gearbox, and a 60 mAh battery. This standard configuration was used for straight-line locomotion, turning, slope traversal, terrain tests, the open-area course, and the confined task. Two configuration changes were used only for dedicated characterizations. A three-stage gearbox replaced the single-stage gearbox in the high-torque payload test while retaining the 60 mAh battery, and a 1000 mAh battery with a mass of 15.7 g replaced the 60 mAh battery in the long-distance tests while retaining the single-stage gearbox. Consequently, the highest trial-averaged speed, the 250-g dedicated payload result, and long-distance performance are reported as configuration-specific measurements rather than as a single operating point.

Preliminary prototype screening also showed that spherical feet were susceptible to lateral drift, whereas the selected C-shaped feet produced more repeatable forward progression under the tested conditions (Supplementary Fig. 3). Preliminary empirical screening indicated that spherical feet were susceptible to lateral drift due to point contact, whereas the selected C-shaped feet produced more repeatable forward progression. The C-shaped feet were therefore adopted for all subsequent quantitative experiments.

Single-DOF coupled transmission and trajectory validation

The transmission combines a crank-rocker with a three-branch, two-DOF parallel mechanism (Supplementary Fig. 2A, B). Continuous motor rotation is converted into periodic rocker motion, and a fixed mechanical relationship between the two parallel-mechanism inputs maps the rotary input phase to a periodic spatial foot trajectory. This mechanical coupling reduces the number of independently commanded transmission inputs and the associated phase-coordination variables, but prevents real-time modification of the foot trajectory. The integrated sensing, communication, and actuation architecture is shown in Supplementary Fig. 2C, and the mechanism motion is shown in Supplementary Movie 1.

Trajectory design considered forward excursion, vertical lift, lateral excursion, lower-branch geometry, and packaging constraints rather than maximizing stride length alone. Candidate dimensions were screened offline with a heuristic genetic-algorithm objective. Mechanism geometry and notation are provided in Supplementary Fig. 5 and Supplementary Table 1, the inverse solution is summarized in Supplementary Fig. 6, and the optimization workflow and representative selection results are shown in Supplementary Figs. 7 and 8. Search bounds, algorithm settings, and the final engineering-selected parameters are given in Supplementary Tables 2–4. The final manufactured geometry also accounted for motor placement, SCM tolerances, assembly clearance, interference avoidance, and space for onboard modules.

To validate the geometric output, the outer body frame was used as a common scale reference to align the model and measured side-view images, and the foot-trajectory contour was extracted in the x-z plane (Supplementary Fig. 4A and Supplementary Movie 1). The modeled and measured trajectories agreed in overall closed shape and principal direction. Relative errors between measured and theoretical effective stride length and maximum lift height were 0.9% and 2.6%, respectively, demonstrating the high fidelity of our kinematic model.

Baseline locomotion and turning performance

With the standard configuration at a 3 V drive condition, the robot achieved a highest trial-averaged unloaded forward speed of 36.9 cm/s over the 40-cm test distance, corresponding to approximately 6.2 body lengths per second (BL/s) for the 6-cm body length (Fig. 2A, Supplementary Fig. 4B, and Supplementary Movie 2). To characterize repeatable locomotion performance across drive conditions, 10 straight-line trials over a 50-cm measurement distance were performed at each commanded voltage from 1.5 to 3 V. The mean forward speed increased from 17.40 cm/s at 1.5 V to 27.72 cm/s at 3 V (Fig. 2A); plotted points represent the trial means and error bars denote ± 1 sample SD. The separate 40-cm trial is not included in the 50-cm voltage-dependent means. The difference between the 40-cm high-speed trial (36.9 cm/s) and the 50-cm series (27.72 cm/s at 3 V) reflects path straightness rather than a change in actuation: over longer runs the robot accumulates small heading deviations that the onboard PID controller compensates for, and the associated steering transients reduce the net forward speed.

The 40-cm value is therefore a short-run peak average, and the 50-cm series a steady-state average that includes heading correction. The measured rotational response of the assembled drive/transmission setup at the commanded voltages is provided in Supplementary Table 5.

Near-pivot turning was produced by differential or counter-rotation of the left and right drives. Across 10 target 90° trials, the measured angles were 109°, 103°, 67°, 80°, 92°, 115°, 79°, 92°, 80°, and 95°, yielding 91.2° ± 15.0° (mean ± sample SD) and a mean absolute error of 12.0° (Fig. 2B, C). A representative approximately 90° turn required about 0.13 s, corresponding to an angular speed of approximately 12.2 rad/s and a turning radius below 1 cm (Supplementary Movie 2). The dispersion indicates rapid small-radius orientation adjustment rather than high-precision turning.

Slope traversal, payload capacity, and structural robustness

Slope tests quantified the boundary of net uphill locomotion for the standard configuration. Five trials were performed at each of 3°, 5°, 6°, and 7°. Mean net speeds were 20.0, 8.0, and 8.75 cm/s at 3°, 5°, and 6°, respectively. At 7°, brief upslope motion was followed by net downslope displacement, giving a mean net speed of -3.1 cm/s (Fig. 2D, and Supplementary Movie 2). The mean net uphill speeds were measured at 3° to 6° slopes, with the stable climbing boundary identified at approximately 6°.

Dynamic payload was evaluated separately for the standard and dedicated high-torque configurations. With the single-stage gearbox, measured speeds were 29.6, 26.7, 16.7, 19.2, and 15.3 cm/s at payloads of 10, 20, 30, 40, and 50 g, respectively (Fig. 2E and Supplementary Fig. 4D). The 50-g condition corresponds to approximately 2.6 BL/s for a 6-cm body length; at 60 g, effective forward locomotion was lost. Replacing the single-stage gearbox with the dedicated three-stage high-torque unit enabled continuous locomotion with payloads from 50 to 250 g. Measured speeds were 5.7, 5.6, 4.5, 3.8, and 3.6 cm/s at 50, 100, 150, 200, and 250 g, respectively (Fig. 2F and Supplementary Fig. 4E). The speed at 250 g corresponds to approximately 0.6 BL/s. At 300 g, locomotion was substantially degraded, with a measured speed of 1.3 cm/s; effective locomotion was not achieved at 400 g. The 250-g value is therefore an upper payload characterization for the dedicated high-torque setup and not the payload of the routine operating configuration.

Quasi-static compression was tested on three independently fabricated prototypes (Fig. 2G–I, Supplementary Fig. 4C, and Supplementary Movie 3). All three reached a common demonstrated load of 12 N without fracture or loss of mechanical function. The tests were intentionally stopped after the onset of geometric bottoming and the associated stiffness increase, so terminal forces are not interpreted as ultimate strengths. After unloading, each prototype retained a low-load compression response. Mean before- and after-loading curves and horizontal ± 1 sample-SD displacement error bars are shown in Fig. 2I; individual responses and the complete test protocol are provided in Supplementary Note 7 and Supplementary Fig. 9. These results establish repeatable load bearing and recovery at the demonstrated condition, not destructive strength or cyclic compression life. Representative standard and high-torque

payload trials are shown in Supplementary Movie 3, with the configuration change identified in the movie.

Environmental adaptability and open-area mobility

Terrain tests evaluated surface transitions, loose support, and local geometric discontinuities (Fig. 3A). Each condition was repeated 10 times, with success defined as completing the prescribed segment without physical intervention and remaining capable of continued locomotion. The synthetic track-grass-track transition had a 90% success rate, with failure caused mainly by tipping at the transition. Loose sand had an 80% success rate because local sinkage produced ineffective foot cycling. The cobblestone-slab transition and the artificial approximately 1-cm gap/obstacle tests each had a 100% success rate. Representative terrain sequences and a continuous segment of repeated indoor-obstacle attempts are provided in Supplementary Movie 4. The repeated-attempt segment is shown at 2-times playback speed and retains manual repositioning between attempts.

The open-area course tested continuous teleoperated path execution on nonideal ground using the standard configuration (Fig. 3B). The approximately 3 m × 1.5 m course required the robot to circumnavigate three markers and pass through a 10-cm-wide passage. The operator issued forward and turning commands using wireless visual feedback; no physical correction or righting was allowed. Overhead video was used only for calibration and offline trajectory reconstruction. All five trials were successful, with completion times of 60, 63, 68, 65, and 57 s, giving 62.6 ± 4.3 s (mean ± sample SD). The experiment demonstrates repeatable teleoperated path execution but not autonomous navigation (Supplementary Movie 5). Movie S5 presents three of the five trials, with onboard-camera footage included for the first displayed trial only.

Long-distance operation and flexure-hinge durability

Early long-distance tests revealed a durability limitation that was not apparent in short bench experiments. A polyimide (PI) universal-flexure hinge experienced combined cyclic bending and shear from foot impacts, mechanism torsion, and the added battery load. In early runs with the original abrupt edge geometry, hinge fracture was observed after approximately 100 to 200 m. A semicircular edge transition was therefore added at the rigid-flex interface without changing the hinge center or nominal mechanism kinematics (Fig. 4A–D). The modification was intended to smooth the local geometry and reduce edge-initiated crack formation; it was an engineering reinforcement rather than a quantified fatigue-life optimization.

Long-distance operation used a 1000 mAh battery with a mass of 15.7 g and the standard single-stage gearbox. Three independently fabricated prototypes, distinct from the compression-test specimens, each completed one prescribed lap in lane 2 of the athletics track, corresponding to approximately 407 m, or roughly 6800 body lengths (Fig. 4F–H and Supplementary Movie 6). The modified hinge remained functional in all three runs, and no hinge fracture preventing locomotion was observed. The

representative R1 run finished in 43 min 10 s; R2 and R3 finished in 42 min 43 s and 43 min 24 s, respectively. Across the three prototypes, the mean overall speed was 0.157 ± 0.001 m/s (mean ± sample SD). The tests were conducted at ambient temperatures of 29°C (R1 and R2) and 31°C (R3), with the battery voltage in R1 falling from 4.2 to 3.68 V over the lap. Because each run was stopped at the prescribed distance rather than at battery depletion, these data demonstrate repeatable 407-m operation rather than a maximum range. Trial-level checkpoint times are provided in Supplementary Table 6.

Confined-space task performance

The confined task evaluated whether locomotion, orientation adjustment, visual feedback, target interaction, and loaded return could be combined into a single teleoperated workflow (Fig. 5 and Supplementary Movie 7). The task used an extended-leg version of the robot to provide approximately 2.3 cm of underbody clearance for the test tube; the drive and power system remained the standard 610 coreless-motor, single-stage, 60 mAh configuration. The extended legs increased ground clearance but also raised the center of mass, increasing susceptibility to tipping during abrupt startup.

The robot traversed an approximately 11-cm-wide passage, approached and magnetically acquired the test tube, transported it through an approximately 8-cm-high low-clearance region, and returned with the payload. The operator primarily used direct visual observation when the robot was visible and relied on the onboard-camera image when the low-clearance structure partially occluded the robot. No physical intervention by the operator was permitted during a trial.

Eight of 10 trials completed the full operational sequence, corresponding to an 80% success rate. One failure resulted from tipping after excessive startup speed and the other from collision with the test tube during approach, which displaced the magnetic module from the intended attachment position. The eight successful trials had a mean completion time of approximately 42 s. Figure 5 shows a representative successful trial completed in 34.6 s. Success rate was the primary outcome, and total completion time is reported as a secondary measure. Repetition counts, scenario-to-design mapping, system specifications, and principal outcomes are consolidated in Supplementary Tables 7–10.

Discussion

The primary contribution of our work extends beyond mere metric optimization; it establishes a fundamental system-level trade-off strategy in microscale robotics. By coupling the two input branches of a parallel mechanism through a fixed crank-rocker relationship, we replace active phase coordination with a deterministic geometric constraint: a single rotary input now generates the full spatial foot trajectory, reducing the control problem from two independent inputs to one. This reduction in actuation dimensionality inherently minimizes wiring complexity, control overhead, and mass, thereby freeing up the critical payload budget for onboard sensing and task modules. Our experimental results on 407-meter continuous locomotion and confined-space manipulation reveal that mechanically coordinated

locomotion can serve as a highly reliable, load-bearing foundation. This shifts the design paradigm from maximizing agility in isolation to maximizing functional integration for real-world deployment.

System-level implications of mechanical coupling

The savings in wiring, control channels and drive hardware follow from this design rather than from a measured comparison with a two-input baseline; quantifying them would require an ablation against an otherwise equivalent mechanism. The experiments indicate that this low-dimensional locomotion base can coexist with sensing, wireless communication, onboard power, and a task module. The standard configuration demonstrated a highest trial-averaged speed of 36.9 cm/s, rapid near-pivot turns, a 50-g transported payload, multi-terrain traversal, and teleoperated tasks. Structural characterization showed a common 12-N demonstrated compression load across three prototypes. These capabilities were not optimized independently: the same frame and transmission must provide locomotion geometry, load paths, and interfaces for the onboard modules. The results therefore support an integration-oriented design strategy rather than a claim of best performance in any single metric.

Operating tradeoffs and comparison with related robots

Speed, payload, and endurance measurements correspond to different operating conditions and should not be combined into a single peak-performance state. The routine configuration used a 60 mAh battery and single-stage gearbox, whereas the 250-g payload was obtained only with the three-stage high-torque gearbox and the approximately 407-m runs used the larger 1000 mAh battery. The gearbox tradeoff is visible directly: the three-stage configuration extends load transport but reduces speed. Likewise, the larger battery enables sustained operation with a battery mass of 15.7 g, approximately 14.0 g more than the 1.7-g baseline battery.

Figure 6 places the baseline standard configuration within the performance space of selected terrestrial robots of similar scale[1–18,24–30]. To avoid mixing configurations in the comparison, the point for this work uses the 50-g transported payload demonstrated with the standard single-stage gearbox in Fig. 6A, the highest trial-averaged forward speed of 36.9 cm/s measured over the 40-cm high-speed trial in Fig. 6C, and a dimensionless cost of transport (COT) of approximately 24.48 with the camera inactive in Fig. 6B. The dedicated 250-g high-torque result remains a separate characterization in Fig. 2F and is excluded from Fig. 6. In panels A to C, open circles denote untethered configurations and filled circles denote tethered configurations; the filled star denotes this work. Cross-platform values should still be interpreted cautiously because actuation, test surfaces, tethering, payload definitions, and power-accounting boundaries differ; Supplementary Table 11 provides the underlying values and source-specific notes.

To complement the metric-specific comparisons in Fig. 6, Fig. 6D presents a level-based five-dimensional performance pentagon for the present robot and four representative platforms: the BHMbot, PLioBot, the quadruped piezoelectric robot, and the biomimetic tripedal piezo robot. The five dimensions are payload capacity, forward speed, compactness, environmental capability, and functional integration.

The three quantitative dimensions are converted to levels L1 to L5 using the value ranges defined in Supplementary Table 12, whereas environmental capability and functional integration are assigned from source-reported demonstrated capabilities using explicit level definitions provided in Supplementary Table 12. The environmental-capability and functional-integration axes both include task execution and are therefore not independent. The pentagons are intended to visualize the breadth and distribution of demonstrated capabilities rather than to produce an overall ranking under identical test conditions. Within this framework, the present system reaches L4 in payload capacity, L4 in forward speed, L3 in compactness, and L5 in both environmental capability and functional integration, under the rubric defined for this comparison.

Long-distance performance is reported using different metrics across the literature. S²worm estimated an allowable travel distance of approximately 208 m from stored energy and measured energy per meter rather than by completing a continuous 208-m run[5], whereas the electrostatic-footpad soft robot directly traveled 31 m over 19 min in an endurance experiment[31]. Other platforms report operating time rather than accumulated terrestrial distance. The three approximately 407-m runs here are therefore reported as directly measured distances under a defined load and surface, in contrast to ranges extrapolated from stored energy.

Teleoperation and field-use boundaries

Teleoperation allowed high-level target recognition and local path decisions to remain with the operator while the robot provided locomotion, image transmission, and IMU-assisted heading regulation. This division is appropriate for testing whether the mechanical platform can support integrated operations without imposing the computing and energy cost of fully onboard autonomy. However, task performance depends partly on the operator and communication link. The open-area and confined-space results therefore demonstrate teleoperated mobility and task execution, not autonomous navigation. Separating platform performance from operator and control effects would require quantitative measurements of communication latency, command frequency, operator variability, and trajectory error.

The magnetic pickup module illustrates a similar system tradeoff. Its small mass and passive attachment simplify integration, but it requires a compatible ferromagnetic interface and does not provide dexterous grasping. The fixed quadruped morphology likewise supports load bearing and module mounting but cannot narrow its lateral body width as CLARI and mCLARI can[9,10]. The proposed platform should thus be viewed as one design point in the trade space between adaptability, manipulation complexity, onboard integration, and locomotion performance.

Limitations and outlook

Several limitations bound the present conclusions. Field-relevant tests were performed on an athletics track, grass, loose sand, paved discontinuities, and an artificial confined environment rather than random rubble or prolonged deployment with severe communication occlusion. Turning accuracy (± 15° at a 90° target) is adequate for the demonstrated tasks, but the current PID-based heading correction introduces

steering transients that reduce net forward speed over long distances; this penalty would be mitigated by a fully closed-loop visual-inertial odometry system. The single-DOF foot trajectory cannot be modified during operation, and the mechanism-complexity benefit has not been quantified against an otherwise equivalent two-input prototype. Compression tests established a common 12-N demonstrated load but did not measure destructive strength or cyclic compression life. Each of the three long-distance prototypes completed one prescribed lap rather than being operated to battery depletion or structural failure, and continuous current and motor-temperature histories were not collected across all runs. Furthermore, hinge durability was evaluated through single continuous long-distance runs for each design, without dedicated cyclic fatigue testing.

Task reliability was also limited by startup transients, body stability, and target alignment. The magnetic module restricts target compatibility, and the current trajectory validation is two-dimensional and geometric rather than phase resolved. Together with the lack of a mechanism ablation, destructive or cyclic compression testing, and full-range endurance measurements, these constraints define the present evidence boundary. The results support the central conclusion that mechanically coordinated insect-scale locomotion can coexist with onboard sensing, substantial load transport, sustained operation, and a complete teleoperated pickup-and-return workflow, while leaving autonomy, adaptive gait control, and lifetime characterization outside the demonstrated scope.

Methods

Experimental design and statistical reporting

Experiments were organized as controlled performance characterization followed by integrated field-relevant validation. Unless otherwise stated, locomotion experiments used 610 coreless motors, a single-stage gearbox, and a 60 mAh battery. The dedicated high-torque payload test retained the 60 mAh battery but used the three-stage gearbox. Long-distance tests retained the single-stage gearbox but used the 1000 mAh battery. The voltage-dependent straight-line speed series used 10 trials at each commanded drive voltage; the target-turning test used 10 trials; slope tests used five trials per inclination; terrain tests used 10 trials per condition; the open-area course used five trials; and the confined task used 10 trials. Compression/recovery and long-distance experiments each used three independently fabricated prototypes, with distinct specimen sets. Unless otherwise stated, dispersion is reported as sample SD over independent trials; no inferential hypothesis testing was applied. Additional repetition counts and outcome definitions are given in Supplementary Table 7.

SCM fabrication and assembly

The body and transmission were fabricated by smart composite microstructures using laser-machined carbon-fiber layers laminated with polyimide films. Carbon-fiber layers provide rigid load-bearing links and mounting interfaces, whereas the polyimide layers form compliant flexures. Components were

released, folded, aligned through slot-and-tab features, and bonded with adhesive. The crank-rocker, parallel mechanism, and leg-foot assemblies were joined to maintain relative joint positions while controlling mass. An overview of the material stack-up and assembly process is provided in Supplementary Note 1 and Supplementary Fig. 1.

Transmission modeling and trajectory validation

A fixed frame was attached to the stationary platform and a moving frame to the parallel-mechanism platform. Candidate moving-platform poses were parameterized by α and β. The inverse-kinematic map returned the two parallel-mechanism input angles, which were mapped through the crank-rocker relationship to the corresponding rocker angles. Candidate poses were retained only when the fixed mechanical coupling relation and geometric feasibility conditions were satisfied; the foot endpoint was then calculated from the leg-linkage geometry. A custom genetic algorithm screened dimensional parameters using forward, lateral, and vertical trajectory excursions together with lower-trajectory feasibility and centering terms. The kinematic workflow, symbols, search bounds, algorithm settings, and selected parameters are given in sections S3 and S4 and Supplementary Tables 1–4.

For image-based trajectory validation, a side-view camera recorded the moving foot and body frame. The outer body frame served as the scale and alignment reference between the model and measured images. The closed foot contour was extracted in the x-z plane, and measured effective stride length and maximum lift height were compared with their theoretical counterparts. Because input phase was not synchronized with pointwise image samples, only geometric trajectory measures were compared.

Actuation, power, and control hardware

All locomotion experiments used 610 coreless motors rated for 3 V. The single-stage gearbox was the default transmission; the three-stage gearbox was used only for the dedicated high-torque payload characterization. The ESP32 controlled the left and right drives, acquired IMU data at approximately 30 Hz, and handled wireless communication. Unit-to-unit motor variation and assembly differences produced heading drift under open-loop drive, so the controller used startup yaw as a reference and applied proportional-integral-derivative (PID) corrections to left-right drive commands. The CMOS camera supplied forward visual feedback. The baseline battery was 60 mAh with a mass of approximately 1.7 g; the long-distance battery was 1000 mAh with a mass of 15.7 g. For the COT estimate, battery-side voltage and current were approximately 3.7 V and 0.5 A at a 3 V motor-drive command, giving an estimated COT = $P/(mgv)$ of approximately 24.48 for $P = VI$, $m = 0.0209$ kg, $g = 9.8$ m/s², and $v = 0.369$ m/s. The camera was inactive during this measurement.

Locomotion, turning, slope, and payload tests

Straight-line speed was calculated from the measured traversal distance and elapsed time on a level surface. The high-speed trial annotated in Fig. 2A used a 40-cm measurement distance and is reported as a single trial-averaged speed. The voltage-dependent series shown in Fig. 2A used a 50-cm measurement distance; 10 repeated trials were performed at each commanded drive voltage, and each plotted point is the mean across those trials. Turning tests commanded an approximately 90° near-pivot maneuver and measured the achieved heading change from video. Slope trials started with the robot facing upslope; net displacement over an effective approximately 35-cm segment defined the signed speed, with positive values indicating uphill progression. Five trials were performed at each slope angle. Only condition means were retained for the slope series, so per-angle dispersion is not reported. For dynamic payload tests, masses were added to the robot and continuous effective forward locomotion was assessed. The single-stage series used 10 to 60 g payloads; the dedicated three-stage series extended the test through 400 g. Representative locomotion and payload videos are provided in Supplementary Movies 2 and 3.

Quasi-static compression tests

Three independently fabricated prototypes were tested with an Instron 5965 universal testing machine. An 80-mm-diameter circular upper platen compressed the robot against a 120-mm-diameter lower platform at 0.01 mm/s, with force-displacement data sampled at 50 Hz. Each prototype was first measured under a nominal 2-N low-load compression, then compressed until geometric bottoming produced a sharp increase in local force-displacement slope. The machine ceiling was 20 N, but tests were manually stopped after bottoming and before destructive failure. After unloading, the 2-N measurement was repeated. Force baselines, displacement referencing at 0.1 N, bottoming detection, interpolation, and mean ± sample-SD processing are described in Supplementary Note 7; raw data and the plotting script are supplied with the supplementary package.

Terrain and open-area tests

For foot-geometry selection, spherical and C-shaped feet were preliminarily compared during forward locomotion on a level surface, leading to the adoption of the C-shaped design due to its superior directional stability. Subsequent terrain evaluations utilized a suite of standardized conditions, including a synthetic track-grass-track transition, loose sand, a cobblestone-slab transition, and artificial approximately 1 cm gap/obstacle fields. A trial was scored as successful only if the robot completed the prescribed segment autonomously without physical intervention, while maintaining continuous locomotion. For the open-area course, the robot traversed an approximately 3 m × 1.5 m region, circumnavigated three markers, and passed through an approximately 10-cm-wide opening. the robot was controlled exclusively via the wireless interface and onboard camera, while external overhead video was recorded independently for post-hoc trajectory reconstruction and trial timing.

Long-distance protocol

Three independently fabricated robots used the same single-stage gearbox, 1000 mAh battery specification, modified flexure-hinge geometry, and lane-2 athletics-track course. Each robot was assigned one approximately 407-m lap and was stopped after completing that prescribed distance. Elapsed times were extracted at 0, 100, 203.5, 303.5, and 407 m from video. Ambient temperature was 29°C for R1 and R2 and 31°C for R3. The test did not use battery depletion or structural failure as a termination criterion. Complete checkpoint data and reporting conventions are provided in Supplementary Note 8 and Supplementary Table 6.

Teleoperation and confined-space task

During teleoperation, the operator provided target recognition, local path selection, and motion commands. Direct visual observation was used when available; onboard-camera images became the primary reference when the robot entered the occluded low-clearance region. The IMU-based controller assisted heading regulation but did not autonomously plan the path. The ventral magnetic module passively attached to a ferromagnetic target interface. The confined task used the extended-leg configuration with approximately 2.3 cm underbody clearance and required passage traversal, target approach, magnetic pickup, low-clearance loaded traversal, and return. Success was defined as completion of the full sequence without physical intervention. Total task time was obtained from the recorded trial video from task initiation to completion of the loaded return; complete stage-by-stage timing was not retained.

Declarations

Acknowledgements

The authors thank Hejinsheng Cao and Ji Tang for their assistance and advice on PCB design. This work was supported by the National Natural Science Foundation of China (No. 52405026).

Author contributions

Conceptualization: R.C., S.Q., Y.D.L.

Methodology: R.C., B.G., Y.D.L.

Investigation: R.C.

Visualization: R.C.

Funding acquisition: S.Q.

Project administration: S.Q.

Supervision: B.F., S.Q., Y.D.L.

Writing – original draft: R.C.

Writing – review & editing: R.C., S.Q., Y.D.L.

Competing interests

The authors declare no competing interests.

Data availability

The data that support the findings of this study are available within the paper and its Supplementary Information. Source data for Figs. 1–6 are provided with this paper. Raw quasi-static compression and recovery measurements are provided in Supplementary Data 1; trial-level long-distance checkpoint times in Supplementary Table 6; cross-platform comparison values and level assignments in Supplementary Tables 11 and 12; and the measured speed, payload, turning and slope values in the Source Data file.

Code availability

The custom MATLAB genetic-algorithm and kinematic workflow is provided as Supplementary Software 1. The code was run with MATLAB R2024b. The exact release and random seed of the original representative run were not recorded.

References

1. Baisch AT, Ozcan O, Goldberg B, Ithier D, Wood RJ (2014) High speed locomotion for a quadrupedal microrobot. Int J Robot Res 33:1063–1082
2. Goldberg B et al (2018) Power and control autonomy for high-speed locomotion with an insect-scale legged robot. IEEE Robot Autom Lett 3:987–993
3. Birkmeyer P, Peterson K, Fearing RS (2009) in 2009 IEEE/RSJ International Conference on Intelligent Robots and SystemsIEEE
4. Hoover AM, Steltz E, Fearing RS (2008) in 2008 IEEE/RSJ International Conference on Intelligent Robots and SystemsIEEE
5. Liu Y et al (2022) S²worm: A fast-moving untethered insect-scale robot with 2-DoF transmission mechanism. IEEE Robot Autom Lett 7:6758–6765
6. Liu Y et al (2024) Singularity analysis and solutions for the origami transmission mechanism of fast-moving untethered insect-scale robot. IEEE Trans Robot 40:777–796
7. Liu Z et al (2024) A wireless controlled robotic insect with ultrafast untethered running speeds. Nat Commun 15:3815
8. Ramirez Serrano F, Hyun NP, Steinhardt E, Lechère P-L, Wood R (2025) J. A springtail-inspired multimodal walking-jumping microrobot. Sci Robot 10:eadp7854

9. Kabutz H, Jayaram K (2023) Design of CLARI: a miniature modular origami passive shape-morphing robot. Adv Intell Syst 5:2300181
10. Kabutz H, Hedrick A, McDonnell WP, Jayaram K (2023) in 2023 IEEE/RSJ International Conference on Intelligent Robots and SystemsIEEE
11. Wu Y et al (2019) Insect-scale fast moving and ultrarobust soft robot. Sci Robot 4:eaax1594
12. Ji X et al (2019) An autonomous untethered fast soft robotic insect driven by low-voltage dielectric elastomer actuators. Sci Robot 4:eaaz6451
13. Haldane DW, Peterson KC, Bermudez FLG, Fearing RS (2013) in IEEE International Conference on Robotics and Automation (IEEE, 2013)
14. Lai Y et al (2024) An agile multimodal microrobot with architected passively morphing wheels. Sci Adv 10:eadp1176
15. Zhu Q, Jiang T, Luo Z, Zhu Y, Huang G (2026) A parallel-legged insect-scale robot based on actuation-structure integrated origami mechanism. Microsyst Nanoeng 12:92
16. Wu Y et al (2025) Untethered soft microrobot driven by a single actuator for agile navigations. Nat Commun 16:6842
17. Wu G et al (2024) A piezoelectric driven amphibious microrobot capable of fast and controllable movement. Smart Mater Struct 33:115035
18. Gao Y et al (2025) A centimeter-scale quadruped piezoelectric robot with high integration and strong robustness. Cyborg Bionic Syst 6:0340
19. Wood RJ, Avadhanula S, Sahai R, Steltz E, Fearing RS (2008) Microrobot design using fiber reinforced composites. J Mech Des 130:052304
20. Abondance T, Jayaram K, Jafferis NT, Shum J, Wood RJ (2020) Piezoelectric grippers for mobile micromanipulation. IEEE Robot Autom Lett 5:4407–4414
21. Zhang P, Kamezaki M, He Z, Sakamoto H, Sugano S (2021) EPM-MRE: Electropermanent magnet-magnetorheological elastomer for soft actuation system and its application to robotic grasping. IEEE Robot Autom Lett 6:8181–8188
22. Kim B et al (2025) Insect-scale terrestrial robot capable of untethered environmental monitoring with multisensors. IEEE/ASME Trans Mechatron 30:7395–7405
23. Feng B, Liu Y, Zhang J, Qu S, Yang W (2025) Miniature origami robot for various biological micromanipulations. Nat Commun 16:2633
24. Miao Z et al (2023) Power autonomy and agility control of an untethered insect-scale soft robot. Soft Robot 10:749–759
25. Kim S, Clark JE, Cutkosky MR (2006) iSprawl: design and tuning for high-speed autonomous open-loop running. Int J Robot Res 25:903–912
26. Doshi N et al (2015) IEEE,. in 2015 IEEE/RSJ International Conference on Intelligent Robots and Systems

27. Hoover AM, Burden SA, Fu X-Y, Sastry SS, Fearing RS (2010) in 3rd IEEE RAS & EMBS International Conference on Biomedical Robotics and Biomechatronics (IEEE, 2010)
28. Che J et al (2025) Arc-heating actuated active-morphing insect robots. Nat Commun 16:3014
29. Gao Y et al (2026) Omnidirectional motion of an untethered tripodal microrobot using radial piezoelectric actuators. Nat Commun 17:5946
30. Li J et al (2026) An insect-scale untethered piezoelectric robot with multiple biomimetic features. Cyborg Bionic Syst 7:0525
31. Liang J et al (2021) Electrostatic footpads enable agile insect-scale soft robots with trajectory control. Sci Robot 6:eabe7906

Figures

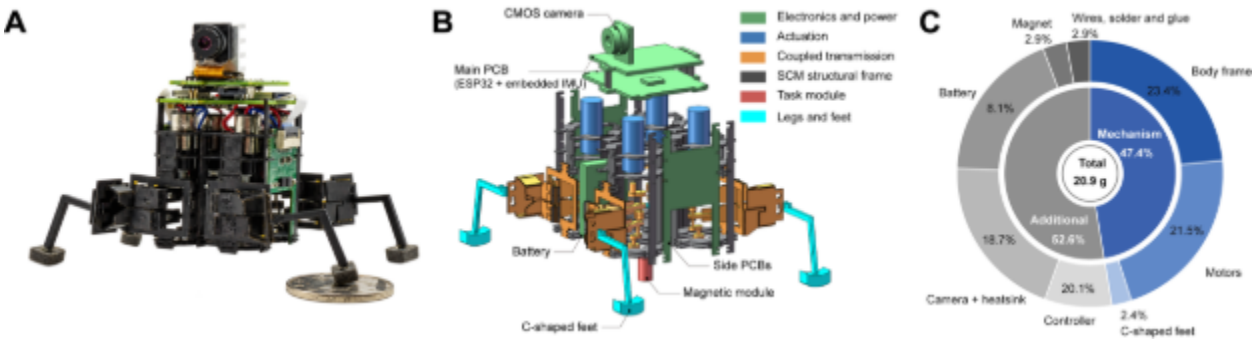


Figure 1

Overall configuration, subsystem integration, and mass distribution of the insect-scale quadruped robot. A Assembled prototype, shown with a coin for scale. **B** Exploded CAD view of the integrated platform; colors denote electronics and power, actuation, coupled transmission, SCM structural frame, task module, and legs and feet. Labels identify the CMOS camera, main PCB with ESP32 and embedded IMU, side PCBs, battery, magnetic module, and C-shaped feet. **C** Mass distribution of the 20.9-g baseline task-integrated prototype. The outer ring shows the component-level mass fractions, and the inner ring groups the mass into mechanism (47.4%) and additional onboard components (52.6%).

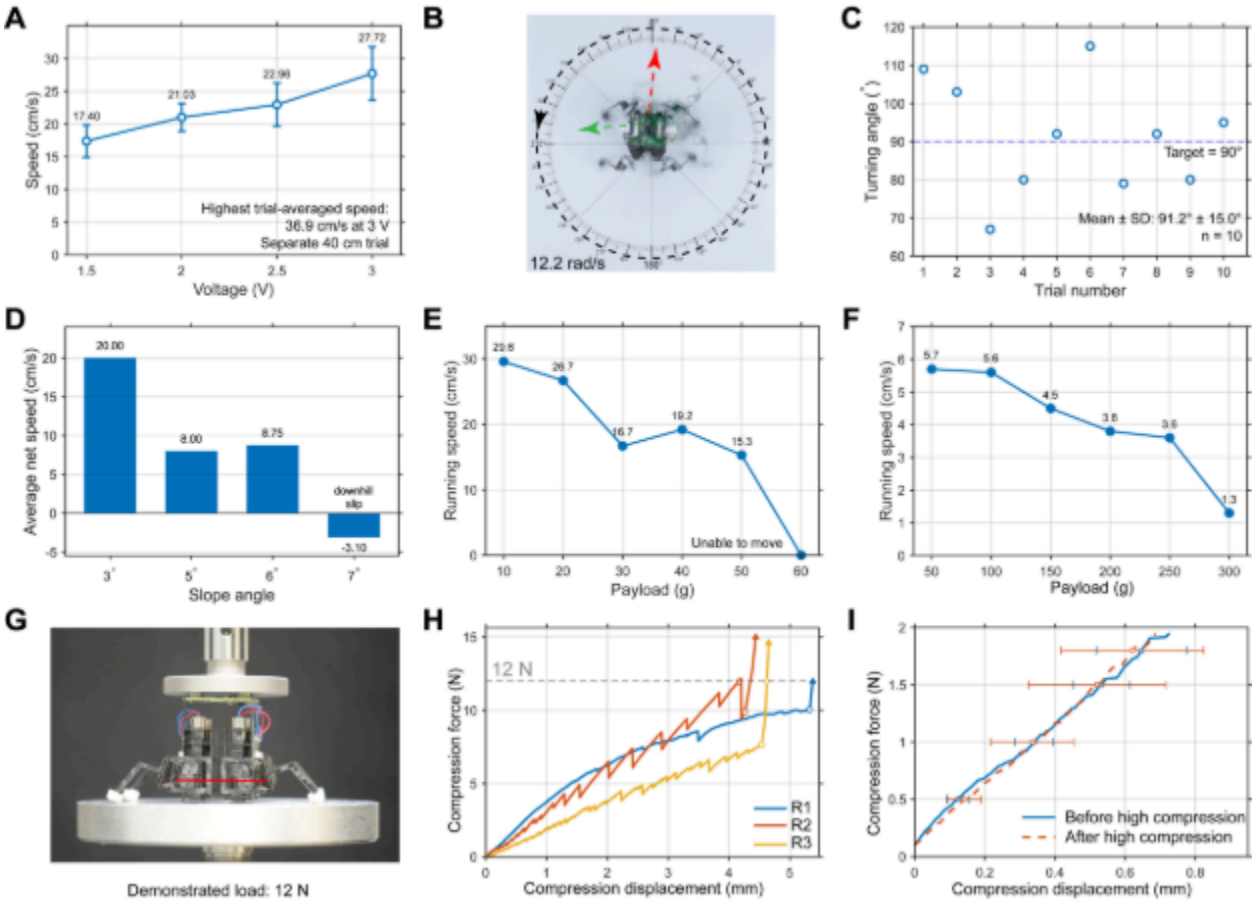


Figure 2

Locomotion, turning, payload transport, and quasi-static compression performance. A Forward speed versus commanded drive voltage for the standard single-stage configuration. Points and error bars denote the mean and ±1 sample SD from 10 trials over a 50-cm measurement distance at each voltage. The annotated highest trial-averaged speed of 36.9 cm/s at 3 V was measured in a separate 40-cm trial and is not included in these means. **B** Representative near-pivot turn with an angular speed of approximately 12.2 rad/s. **C** Achieved turning angles in 10 trials with a target of 90° (dashed line); the mean ± sample SD was 91.2° ± 15.0°. **D**Mean net speed from five trials at each slope angle. Positive values indicate net uphill progression; the negative value at 7° indicates net downslope displacement. Error bars are not shown (n = 5 per angle). **E** Payload–speed relationship for the standard configuration with a single-stage transmission. Effective forward locomotion was lost at 60 g. **F** Payload–speed relationship for the dedicated high-torque configuration with a three-stage transmission. Locomotion was substantially degraded at 300 g. **G**Representative quasi-static compression test at the common demonstrated load of 12 N. **H** Force–displacement responses of three independently fabricated prototypes (R1 to R3). Open circles indicate the onset of geometric bottoming, diamonds mark the common demonstrated load of 12 N (dashed line), and triangles mark experimenter-terminated endpoints. **I** Mean low-load compression responses before and after high compression. Displacement is referenced at 0.1 N; horizontal error bars denote ±1 sample SD across the three prototypes.

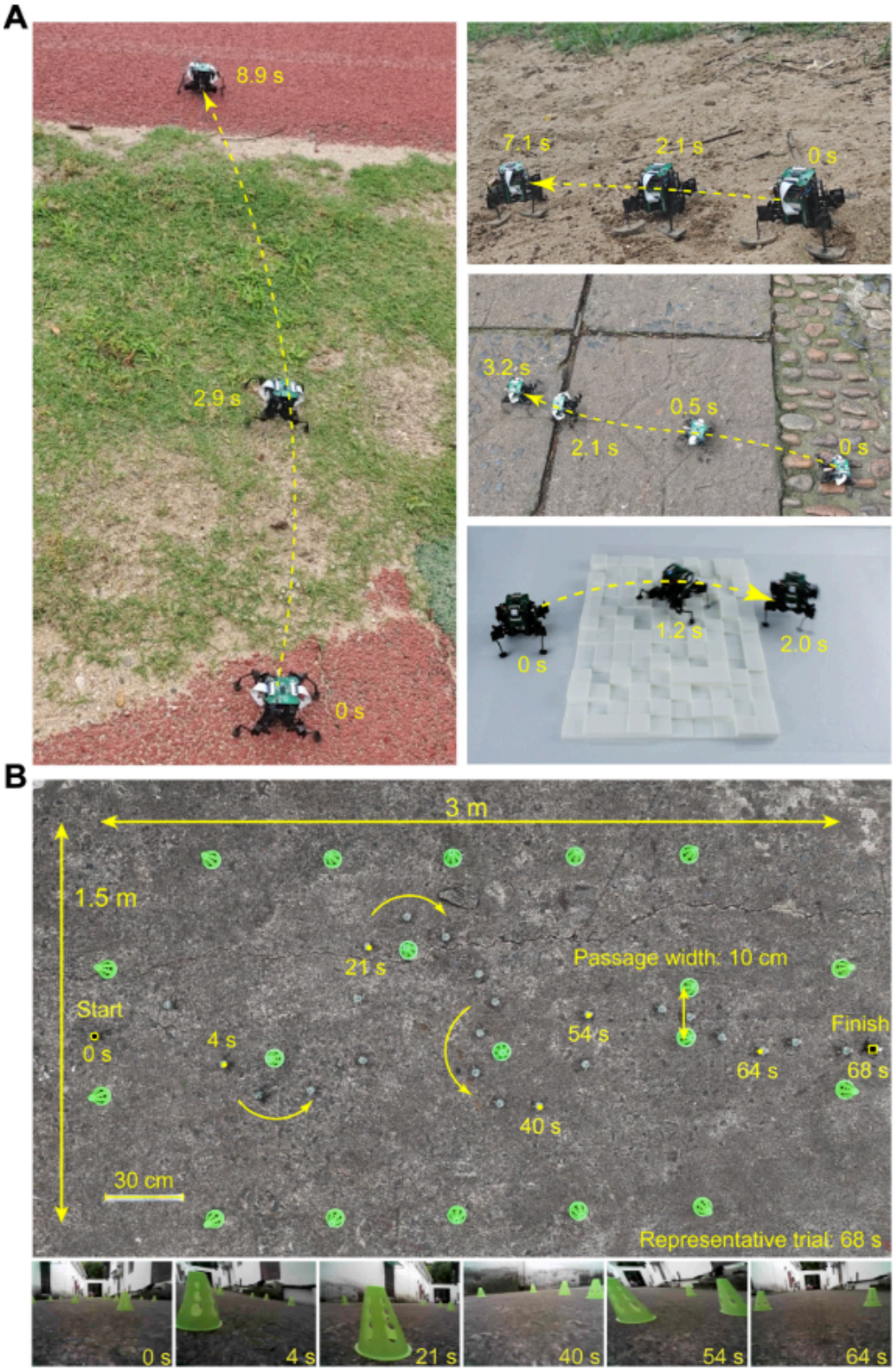


Figure 3

Environmental adaptability and teleoperated open-area mobility. A Representative locomotion across a synthetic track–grass–track transition, loose sand, a cobblestone–slab transition and an artificial obstacle field with approximately 1 cm discontinuities. Yellow dashed arrows indicate the direction of motion, and time labels indicate representative stages. B Open-area marker-circumnavigation and narrow-passage test using the standard configuration. The trajectory over the 3 m × 1.5 m test area with

a 10 cm wide passage is shown with position markers and time labels indicating key stages. Selected onboard-camera frames at 0, 4, 21, 40, 54 and 64 s are also shown. All five trials were successful, with a mean completion time of 62.6 ± 4.3 s (mean ± sample SD).

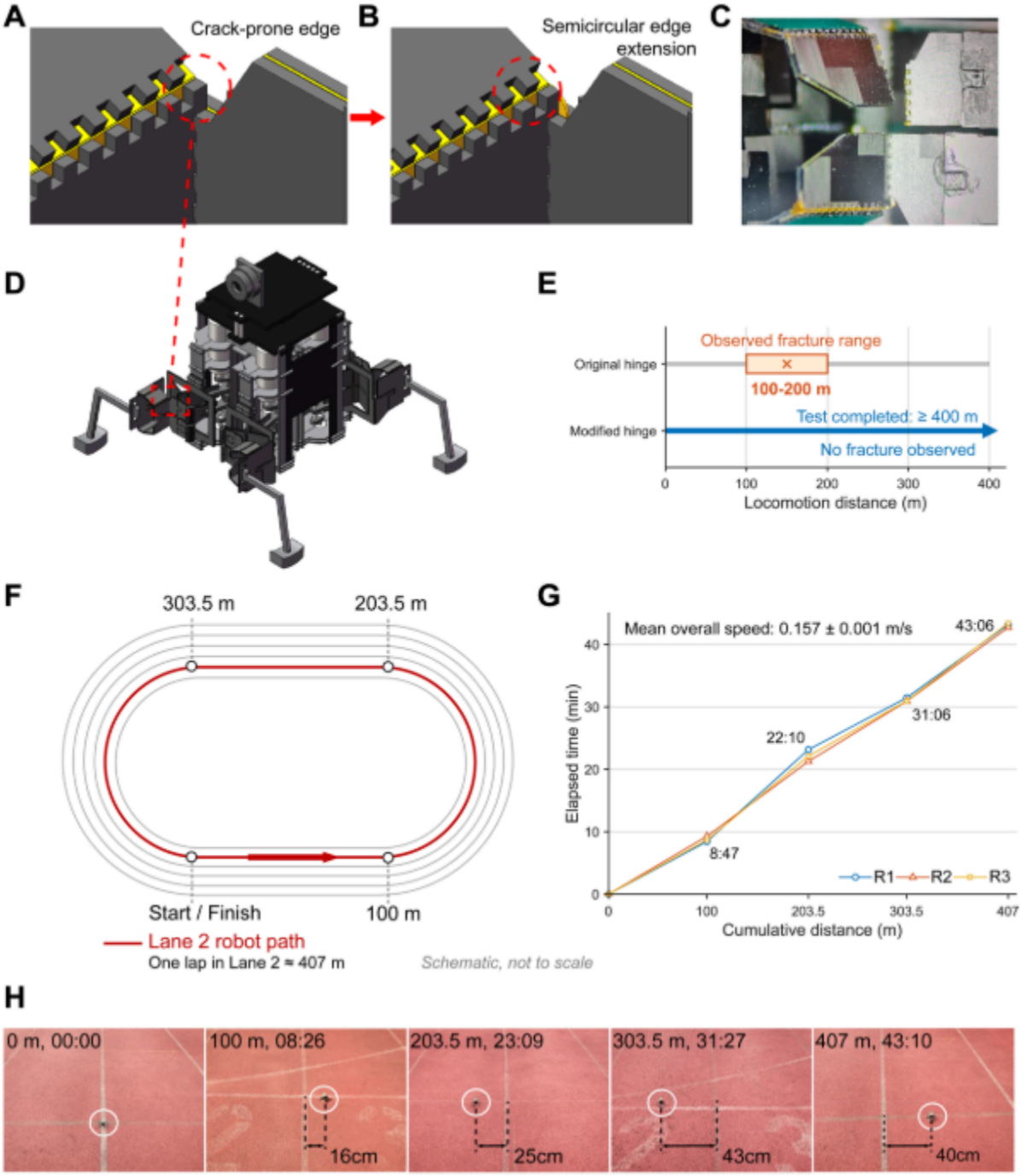


Figure 4

Flexure-hinge reinforcement and long-distance operation with the large-battery configuration. A Crack-prone edge of the original universal flexure hinge. **B** Modified hinge with a semicircular edge extension at the rigid-flex transition. **C** Representative fracture morphology observed in the original hinge after prolonged locomotion. **D**Location of the modified hinge on the robot. **E** Observed long-distance behavior of the two hinge designs. Fracture was observed in early runs with the original hinge after approximately

100 to 200 m, whereas the modified design completed the prescribed ≥400-m test without observed fracture. **F** Schematic of one lap in lane 2 of the athletics track, corresponding to approximately 407 m. **G** Cumulative distance-time profiles for three independently fabricated prototypes (R1 to R3) over the prescribed lap. Markers indicate elapsed time at the designated distance checkpoints, time annotations indicate the mean across the three prototypes, rounded to the nearest **second. H** Representative R1 video frames at 0, 100, 203.5, 303.5, and 407 m. Across the three prototypes, mean overall speed over the prescribed lap was 0.157 ± 0.001 m/s (mean ± sample SD); trial-level checkpoint data are provided in Supplementary Table 6.

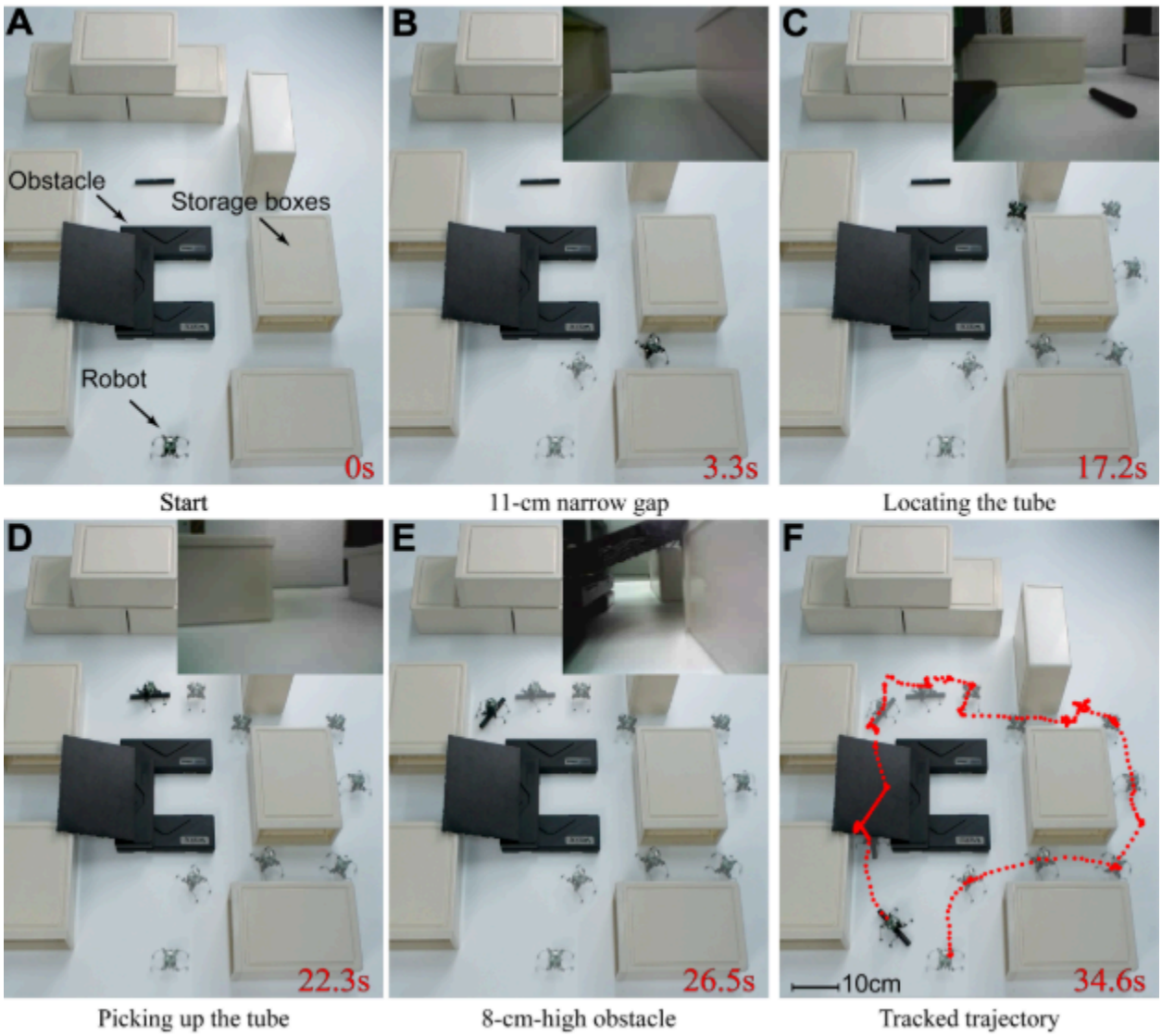


Figure 5

Teleoperated confined-space test-tube pickup-and-return task. A Initial robot position. **B** Traversal of the approximately 11-cm-wide passage. **C** Localization and approach to the test tube. **D** Magnetic pickup of the test tube. **E** Loaded traversal of the approximately 8-cm-high low-clearance region; the inset shows the onboard-camera view used when direct observation was partially occluded. **F** Offline-reconstructed trajectory of the representative successful trial. The labeled times indicate representative task stages,

and the total completion time was 34.6 s. Eight of 10 trials completed the full task, corresponding to an 80% success rate; the mean completion time across the eight successful trials was approximately 42 s.

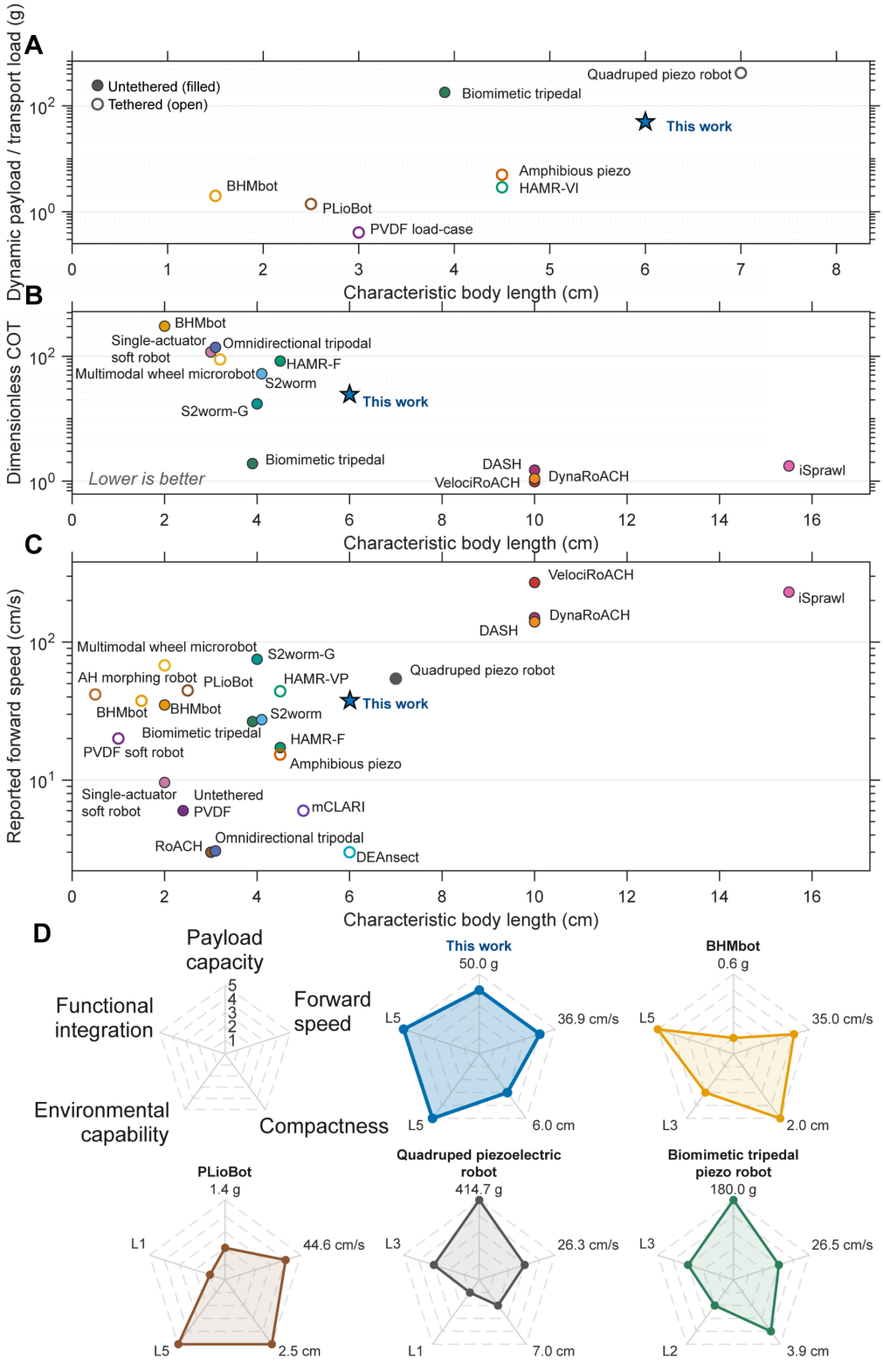


Figure 6

Performance-space comparison with terrestrial robots of similar scale. A Reported dynamic or transported payload versus characteristic body length. The value for this work is the 50-g payload

demonstrated with the standard single-stage configuration. **B** Dimensionless cost of transport, COT = P/(mgv), versus characteristic body length; lower values indicate lower electrical energy use per unit weight and distance within the stated measurement boundary. **C** Reported forward speed versus characteristic body length. Literature points use source-reported maximum or representative values listed in Supplementary Table 11; this work uses the highest trial-averaged speed of 36.9 cm/s measured over the separate 40-cm high-speed trial with the standard configuration. The dedicated 250-g three-stage payload result is excluded from panels A to C. This configuration is excluded because its three-stage gearbox trades speed for load capacity, so the standard configuration provides a like-for-like comparison across platforms. The filled star denotes this work; open and filled circles denote untethered and tethered literature configurations, respectively, and the vertical axes in panels A to C are logarithmic. **D** Five-dimensional performance pentagons comparing this work with the BHMbot, PLioBot, the quadruped piezoelectric robot, and the biomimetic tripedal piezo robot. The axes represent payload capacity, forward speed, compactness, environmental capability, and functional integration. Quantitative values and demonstrated capabilities are assigned to levels L1 to L5 according to the criteria in Supplementary Table 12. Underlying values and configuration notes are provided in tables S11 and S12.

Supplementary Files

This is a list of supplementary files associated with this preprint. Click to download.

- SupplementaryMovie2.mp4
- SupplementaryMovie4.mp4
- SupplementaryMovie7.mp4
- SupplementarySoftware1.zip
- NatureCommunicationsSupplementary.docx
- SupplementaryMovie6.mp4
- SupplementaryMovie1.mp4
- SupplementaryData1.zip
- SupplementaryMovie5.mp4
- SourceData.xlsx
- SupplementaryMovie3.mp4